PAPER • OPEN ACCESS

Extended-MHD simulations of disruption mitigation via massive gas injection in SPARC

To cite this article: A. Kleiner *et al* 2025 *Nucl. Fusion* **65** 026015

View the article online for updates and enhancements.

Extended-MHD simulations of disruption mitigation via massive gas injection in SPARC

A. Kleiner[1,*], N.M. Ferraro[1], R. Sweeney[2,3], B.C. Lyons[4] and M. Reinke[3]

[1] Princeton Plasma Physics Laboratory, P.O. Box 451, Princeton, NJ 08543-0451, United States of America
[2] Massachusetts Institute of Technology, Cambridge, MA, United States of America
[3] Commonwealth Fusion Systems, Devens, MA, United States of America
[4] General Atomics, San Diego, CA, United States of America

E-mail: akleiner@pppl.gov

Abstract

Recent developments to the M3D-C1 code enable higher fidelity modeling of disruptions, and can be applied in the design verification of reactor-scale tokamaks. Among these new capabilities is a method to mesh conducting vessel structures such as coils and passive plates, packing of the toroidal mesh around gas injectors, as well as anisotropic resistivity inside the vessel structures. We present extended-magnetohydrodynamic (MHD) simulations of disruption mitigation via massive gas injection (MGI) in SPARC. The goal of this study is to inform the disruption mitigation layout of SPARC and aid in the design of an effective gas injector configuration. Fully three-dimensional simulations with M3D-C1 are carried out for various injector configurations with the primary goal of determining the effect of different MGI parameters on heat loads and vessel forces. The simulations include a model for impurity ionization, recombination, advection and radiation, as well as spatially resolved conducting structures around the plasma. A localized mixture of deuterium and neon with a small toroidal and poloidal width is injected in up to six locations. We demonstrate that M3D-C1 can model a rapid shutdown via MGI using narrow and more realistic gas plumes than in previous simulations. As a result of the $q = 1$ surface in the SPARC baseline case a sawtooth is observed early in the simulations. Despite the sawtooth and the onset of edge MHD instabilities, the impurity distribution remains localized around the injector locations, but enables a radiative shutdown of the plasma. We find that using the maximum of six gas injectors results in a lower peaking factor and leads to a more even distribution of radiation toroidally than using two injectors.

* Author to whom any correspondence should be addressed.

1. Introduction

Tokamaks are prone to plasma disruptions [1] as a result of magnetohydrodynamic (MHD) instabilities or loss of control [2]. Disruptions are a sudden loss of thermal energy and plasma current. Strong heat loads, especially in the divertor region as well as forces on the vessel occur as a result of disruptions with potential catastrophic effects on the device. Thus, disruptions are a major concern for the operation of tokamaks, especially for reactor-scale machines, where disruptions can shorten the operational lifetime or cause damage to the machine. In order to manage these challenges many efforts aim at prediction, avoidance and mitigation of disruptions. However, not all disruptions can be avoided and therefore mitigation strategies need to be implemented in machine designs. SPARC is a modern tokamak that follows the high-field path [3] to achieve a net fusion energy gain using high-temperature superconducting magnets [4], and is currently under construction by Commonwealth Fusion Systems in Devens, Massachusetts [5]. While the machine is being designed to withstand the forces that are expected during an unmitigated disruption [6], it is estimated that disruptions in SPARC can result in heat flux high enough to melt the surface of the tungsten plasma-facing components [7].

As complete disruption avoidance is very challenging, disruptions are likely to occur in SPARC and the machine needs to be equipped with an effective disruption mitigation system (DMS). Following the successful deployment of massive gas injection (MGI) to mitigate disruptions [8, 9] on many existing tokamaks including Alcator C-MOD [10, 11], and successfully operating as a machine protection system on JET [8], the SPARC DMS will be based on the same method. Besides (shattered) pellet injection [12, 13], MGI has been shown to be effective in the rapid shutdown of plasmas [14] by radiating part of the stored energy. With this goal in mind we present extended-MHD simulations in SPARC with higher fidelity models for the wall region and gas injection. Previous studies of disruption mitigation using various extended-MHD codes have only included an ideally conducting wall [15, 16], parts of the inner wall [17] or a single inner wall only [18, 19], whereas in the present work we will include several wall layers and conducting elements within the wall region to capture eddy currents and wall forces more accurately. Artola *et al* [18] contains a comparison of three extended-MHD codes that are widely used for disruption studies. Note that the model to represent wall elements within M3D-C1 has been updated since the publication of [18], and the updated wall model is described in the present manuscript. Another challenge has been resolving the jets for the injected impurities with previous analysis using toroidally very wide impurity distributions [20], while in our simulations we will use a toroidally packed

mesh that allows for a narrower and thus more realistic gas plume. The results of the simulations presented here inform the MGI layout of SPARC about the optimal injector layout in terms of location and number of injectors. In particular, we are interested in how these parameters affect radiated power, rapid shutdown time, toroidal peaking factor (TPF) and wall forces during a planned shutdown of the plasma via MGI. This also serves as a proof-of-principal study that demonstrates that MGI can be modeled with a realistic size of the gas plume in extended-MHD simulations. For the first time we present simulations of disruption mitigation in the SPARC tokamak.

Projections for the dynamics of a rapid plasma shutdown to mitigate the effects of disruptions can be carried out by means of 3D MHD simulations coupled with a model for atomic physics to treat the dynamics of the impurity species. In this paper we simulate rapid plasma shutdowns in SPARC via MGI using the M3D-C1 code, which has been successfully applied to model disruption dynamics and mitigation in previous studies [15, 19, 21] and has been benchmarked with other 3D MHD codes [16]. This work builds upon the coupling of M3D-C1 with KPRAD [22] using the gas injection capabilities developed before [16], but the present study extends these capabilities by using newly developed abilities to represent further conducting structures and anisotropic resistivity inside these structures, as well as non-equidistant toroidal planes to better resolve the (narrow) gas injection sites. The M3D-C1 code solves a set of extended-MHD equations using advanced meshing utilities that allow for whole device modeling. In the present simulations we are applying recently developed features such as anisotropic resistivity in the wall region to represent ports, and non-equidistant toroidal planes to better resolve the injected narrow gas plumes. While simulations with one to six gas injectors have been carried out, most of the analysis will focus on cases with two and six injectors, representing gas injection at a single toroidal site and at three toroidally equidistant sites, respectively. Note that the final design for SPARC has six injectors at six equidistant toroidal locations alternating top and bottom injection. This decision was influenced by our physics understanding at the time of the decision informed by the simulations reported herein and complementary simulations from the NIMROD code [23], together with engineering considerations regarding SPARC port allocations, diagnostic implications, and space constraints. Future simulation and SPARC experimental work may validate or invalidate the expectation that the 6 valve equidistant toroidal distribution alternating top-bottom leads to the lowest radiation peaking incident on the wall.

This paper is structured as follows: section 2 describes the plasma equilibrium, numerical model including the M3D-C1 extended-MHD equations and impurity model as well as the representation of device components and the computational

mesh. Section 3 presents the rapid shutdown dynamics observed in the studied MGI scenarios. The spatial distribution of impurities and toroidal peaking of radiation are analyzed in section 4. In section 5 we discuss the evolution of flux surfaces and formation of stochasticity throughout the thermal quench (TQ) and current quench (CQ).

2. Plasma equilibrium and numerical model

In this section we describe the SPARC primary reference discharge (PRD) equilibrium, which provides the initial conditions for the rapid shutdown simulations, followed by the physical and numerical model of M3D-C1.

2.1. SPARC equilibrium

The initial conditions for the extended-MHD simulations are given by the SPARC PRD, which is a projected double-null diverted equilibrium with DT fueling in H-mode, maximizing fusion gain [24]. The geometry as well as pressure and safety factor profiles are shown in figure 1. In this paper ψ_N denotes the normalized poloidal flux. While this discharge is projected to operate in H-mode, the profiles do not have a pedestal. The plasma has a geometric major radius of $R_0 = 1.85$ m with the magnetic axis being located at $R_m = 1.89$ m and the LCFS closely follows the inner wall. The central safety factor value is below one, and thus the plasma is prone to developing a sawtooth instability. The initial plasma current is $I_p = 8.8$ MA at an on-axis magnetic field of $B_0 = 12.2$ T, and the initial thermal and in-vessel poloidal magnetic energies are $W_T = 20$ MJ and $W_M = 70$ MJ, respectively.

2.2. Extended-MHD and impurity dynamics model

Nonlinear 3D simulations are performed with the initial value code M3D-C1, which implements an extended-MHD model derived from the Braginskii equations [25]. In particular, the extended-MHD model used in our simulations is given in terms of the equations

$$\frac{\partial n}{\partial t} + \nabla \cdot (n\mathbf{u}) = \Sigma,$$

$$\frac{\partial n_j}{\partial t} + \nabla \cdot (n_j\mathbf{u}) = \sigma_j + D\nabla^2 n_j,$$

$$nm_i\left(\frac{\partial \mathbf{u}}{\partial t} + \mathbf{u} \cdot \nabla\mathbf{u}\right) = \mathbf{J} \times \mathbf{B} - \nabla p - \nabla \cdot \Pi$$
$$+ \mathbf{F} - m\mathbf{u}\Sigma,$$

$$\frac{\partial p}{\partial t} + \mathbf{u} \cdot \nabla p + \Gamma p \nabla \cdot \mathbf{u} = (\Gamma - 1)\left[Q - \nabla \cdot \mathbf{q} + \eta J^2\right.$$
$$\left. - \mathbf{u} \cdot \mathbf{F} - \Pi : \nabla u - \frac{1}{2}m_i v^2 \Sigma\right],$$

$$\mathbf{E} = -\mathbf{u} \times \mathbf{B} + \eta\mathbf{J},$$

$$\mathbf{J} = \frac{1}{\mu_0}\nabla \times \mathbf{B}, \quad \frac{\partial \mathbf{B}}{\partial t} = -\nabla \times \mathbf{E}, \quad (1)$$

with $\Sigma := \sigma + D\nabla^2 n$ and where, as usual, $\mathbf{B}$ denotes the magnetic field, p the pressure and n the main ion density. For an impurity with atomic number $Z n_j$ denotes the density for each charge state with $1 \leqslant j \leqslant Z$. Furthermore, $\mathbf{u}$ is the fluid velocity, $\mathbf{J}$ the current density, $\mathbf{E}$ the electric field, Γ the ratio of specific heats, m_i the main ion mass, η the resistivity, Π the viscous stress tensor, $\mathbf{F}$ are external forces, Q is a heat source term, σ an ion source term and D denotes particle diffusivity. The heat flux density is $\mathbf{q} = -\kappa\nabla T - \kappa_\parallel \frac{\mathbf{BB}}{B^2}\nabla T$ with isotropic thermal conductivity κ, parallel thermal conductivity $\kappa_\parallel$ and temperature T. For further information on the M3D-C1 model equations see [15]. This system of equations is solved in 3D geometry using reduced quintic C^1 finite elements within the poloidal plane and cubic finite elements in toroidal direction [26, 27] with semi-implicit time stepping on an unstructured mesh with triangular elements in the poloidal plane and prism-shaped elements toroidally (see section 2.3 for more details on the mesh). Plasma resistivity is calculated according to the well known Spitzer resistivity model. Equilibrium plasma rotation can in principle be included, but is not considered in this study as it might have introduced further numerical challenges. In our model the stress tensor Π includes the effect of finite viscosity, which has a direct influence on plasma dynamics. The simulations are carried out fully three-dimensional as explained in subsection 2.3. The code uses a cylindrical (R, ϕ, Z) coordinate system, where R is the major radius, ϕ the toroidal angle and Z the vertical distance w.r.t. the midplane.

Atomic processes such as ionization, recombination and radiation are included via the KPRAD module [22], which has been coupled with M3D-C1 [15]. This model does not assume a coronal equilibrium. Instead ionization and recombination determine the impurity charge state evolution. The radiated power, associated with charge state k is calculated as $P_{rad,k} = n_k n_e L_k$, where n_k is the ion density of charge state k, n_e is the electron density and L_k is the radiation rate, which is taken from the ADPAK database [28]. Within this model loss of thermal energy can happen due to ionization, line radiation, bremsstrahlung and recombination radiation. Neutral impurities are injected at zero temperature and brought to the ion temperature T_i upon ionization. KPRAD uses an explicit time step with faster subcycling than a typical MHD time step such that multiple KPRAD time steps are carried out during a single advance of the MHD time step. Changes to the densities of individual ion charge states based on recombination and ionization rates are calculated within KPRAD and enter the M3D-C1 equation through the source/sink terms in the set of equations (1). Advection is calculated within M3D-C1 by solving a PDE during the MHD time step. More details on the coupling between M3D-C1 and KPRAD can be found in [15].

2.3. Meshing & representation of vessel components

M3D-C1 uses an unstructured triangular mesh that can be divided into three distinct areas: (1) a plasma region, where the set of extended-MHD equations (1) is being solved. This region covers the plasma and extends beyond the last closed flux surface (LCFS) to the inner wall. In the region between the
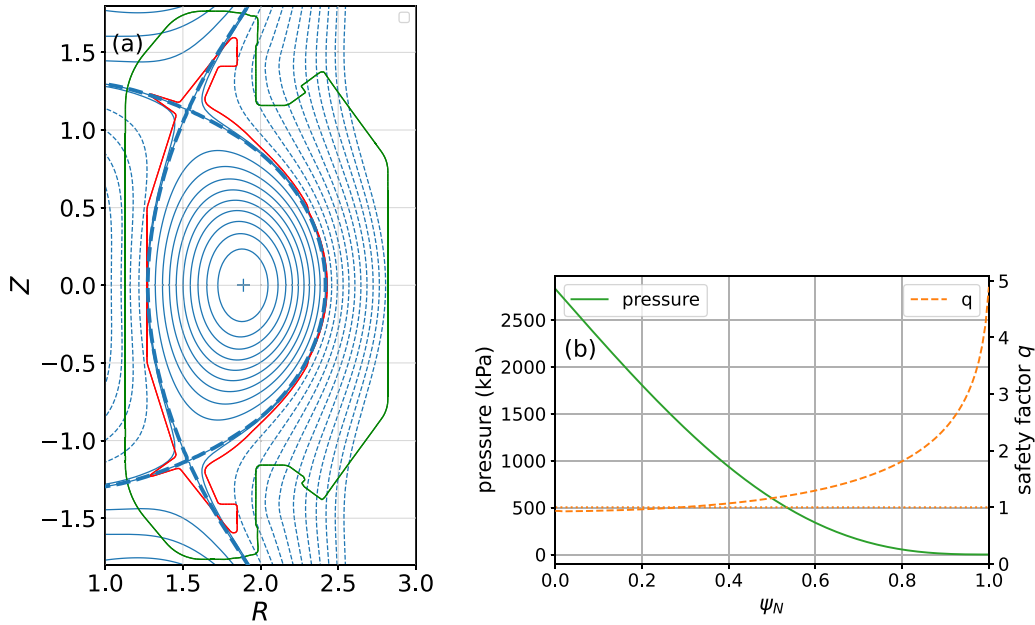
Figure 1. (*a*) Flux surfaces of the initial equilibrium shown together with the inner wall and the outermost shell of the vacuum vessel. (The full mesh and wall structures are illustrated in figure 2.) (*b*) Pressure *p* and safety factor *q* profiles in the SPARC PRD equilibrium used in our disruption mitigation simulations.

LCFS and the first wall, the plasma is considered to have very low pressure and temperature and thus very high resistivity. (2) A resistive wall region. (3) A vacuum region without plasma, but finite electromagnetic fields. Recent developments to the M3D-C1 code enable a more accurate representation of device structures. Unlike in previous studies of disruptions and their mitigation, the wall region is not modeled as a single thin layer, but consists of multiple shells comprised of spatially resolved conducting elements with realistic resistivity values. These three regions of the computational domain together with the device structures that are included in the M3D-C1 model are illustrated in figure 2. Including more conducting elements than only the inner wall allows us to better identify where eddy currents are induced inside the device and enables a more accurate calculation of the wall forces. SPARC has rows of ports at three poloidal locations on the outboard side. These ports are represented in the model in terms of axisymmetric regions of anisotropic resistivity, where the wall material's actual value of resistivity is applied to poloidal currents, but toroidal currents are suppressed by applying vacuum resistivity to the toroidal component of the current density within the port area. At the time when the simulations were carried out the SPARC design featured two passive plates, which are included in the wall model (see figure 2). However, these passive plates have since been removed and are no longer part of the SPARC design. The simulations presented here are fully three-dimensional and use prism-shaped elements in between toroidal planes. The number of toroidal planes used in a particular simulation depends on the number of toroidal injector locations and the toroidal spread of the gas plume, but ranges in between 12 and 24 for the cases presented here. M3D-C1 does not require these toroidal planes to be equidistant, and

in order to better resolve the dynamics around the gas jets and to resolve the strong gradients, toroidal planes are packed around the injector locations as shown in figure 3. During the six injector simulation we increased the number of toroidal planes from 18 to 24 as the injected gas plume was moving toroidally. Two planes were added toroidally at each side of the injector sites to ensure that the strong gradients associated with the injected gas can still be resolved.

2.4. Model for gas injection dynamics & injector layout

One configuration that was considered for the SPARC DMS layout is six gas injector valves at three toroidal locations with an upper and lower gas valve. In the simulations we consider up-down symmetric configurations with six, four and two injectors, as well as up–down asymmetric configurations with one and five injectors. Within the poloidal plane the ends of the MGI barrels are modeled at $R = 2.18$ m and $Z = \pm 0.68$ m. The toroidal location varies depending on the number of injectors. When one or two injectors are used the gas is injected only at a single toroidal position. With four injectors the toroidal spacing is 180°, with five and six injectors the toroidal spacing between injectors is 120°. The injected gas is modeled in terms of a gas plume with Gaussian shape and is toroidally localized. Smaller gas plumes provide a more realistic representation of the injected gas jets and thus allow for a more physical prediction. However, such small impurity plumes are more difficult to resolve in the simulations and require very small time steps in addition to using higher spatial resolution. In the process of finding plume sizes that would be as realistic as possible, but could still be resolved we adopted a half width of the Gaussian of 8 cm in poloidal direction and 80 cm
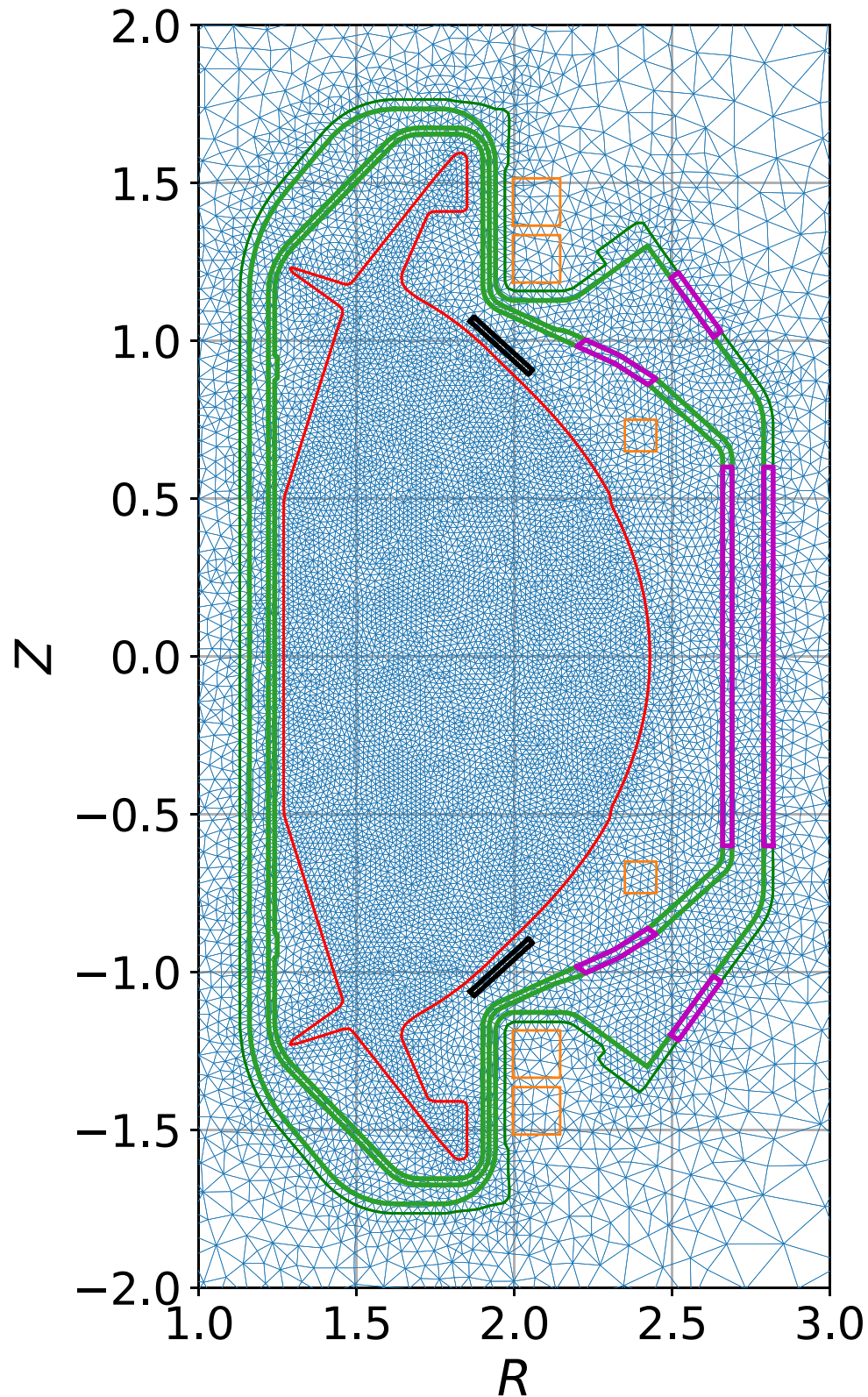
Figure 2. Unstructured mesh showing the plasma region within the first wall (red) with relevant surrounding conducting structures. Two shells of the vacuum vessel are shown in green, and the passive plates in black. The purple lines indicate the location of the ports, where anisotropic resistivity is used. Magnetic field coils are plotted in orange. Note that the poloidal field and center stack coils lie within the computational mesh outside of the shown area.
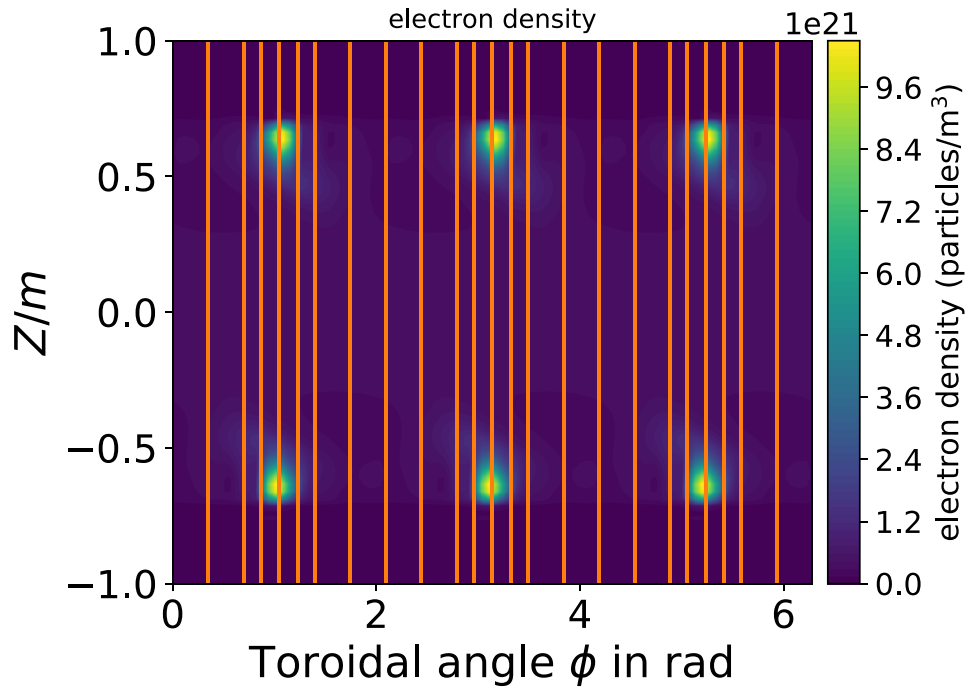
Figure 3. Electron density as a function of the toroidal angle ϕ and Z at fixed $R = 2.18$ m showing the location and size of the gas injectors. The orange lines indicate the position of the 24 toroidal planes, and how they are more densely packed around the injector sites than in between.

in toroidal direction in the simulation with two injectors. In the six injector case we were able to reduce it to 4 cm and 24 cm, respectively. Figure 3 illustrates the injector layout in the simulations using the full six injector layout as an example. The gas plume has zero initial velocity, but is advected by the bulk plasma. At the time when these simulations were carried out the projection was for SPARC to use a mixture of neutral Ne and ionized D in a ratio of 1:10. It is expected that $\sim 10^{22}$ Ne atoms must be delivered in a gas pulse with a duration of 2 ms for successful mitigation of the SPARC PRD. An injection rate of 7.5×10^{23} particles of Ne per second is used which gives near the full delivery with six valves. In our simulations, the impurities are injected beginning at $t = 0$ at the nominal injection rate.

3. Evolution of disruption dynamics

The analysis in this section focuses on the cases with two and six injectors at the same total injections rate of 7.5×10^{23} Ne/s, as these two cases represent injection at a single toroidal plane and at the possible maximum of three toroidal planes. However, simulations with different numbers of injectors and different total injection rates were also performed until the early TQ. Here, each individual gas injector uses the same injection rate, and the total number of injected particles thus scales with the number of injectors. Table 1 provides an overview of the injection rates in each considered case.

Table 1. Injection rates in units of particles of Ne/s are shown for the simulations presented in this paper.

# Injectors	Injection rate per injector	Total injection rate
1	1.25×10^{23}	1.25×10^{23}
2	3.75×10^{23}	7.5×10^{23}
4	1.25×10^{23}	5×10^{23}
5	1.25×10^{23}	6.25×10^{23}
6	1.25×10^{23}	7.5×10^{23}

3.1. MHD, radiated power and thermal energy

The SPARC PRD equilibrium exhibits an on-axis safety factor below unity with a rational $q = 1$ surface at $\psi_N = 0.25$, as seen in figure 1(*b*). This leads to the onset of a sawtooth instability early in the simulations. At the same time, the presence of the gas plumes due to MGI induces a low-n MHD perturbation, where n is equal to the number of toroidal injection locations, i.e. $n = 1$ for two injectors and $n = 3$ for six injectors. The magnetic energy associated with different toroidal modes in these two cases is shown in figure 4. With only two injectors the $n = 1$ mode is dominant as expected from both, the sawtooth, and also the $n = 1$ perturbation introduced by the gas injection in a single toroidal plane. Mode growth is slow during the pre-TQ and amplitudes peak during the TQ. In the six injector case the $n = 3$ mode due to gas injection grows first and shortly after it saturates the $n = 1$ mode becomes dominant. Here, the pre-TQ is defined as the period between the start
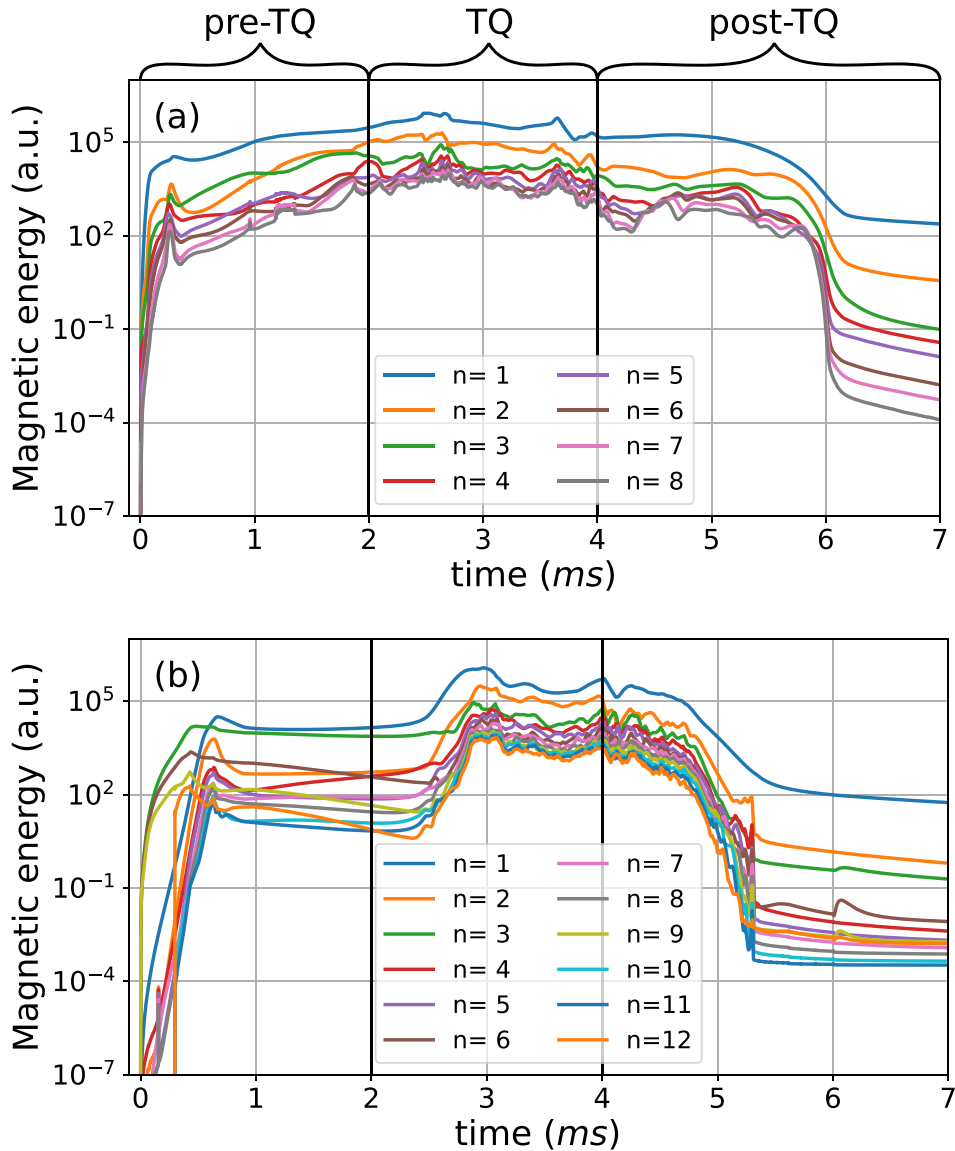
Figure 4. Magnetic energy associated with different toroidal modes. Low-*n* instabilities grow early due to the gas plumes and sawtooth instability. The black lines indicate the approximate beginning and end of the thermal quench, during which strong MHD activity is seen. (*a*) Simulation with two injectors. (*b*) Simulation with six injectors. Both at the same total nominal injection rate of 7.5×10^{23} particles of Ne per second.

of injection and the time when the thermal energy W_{th} starts to drop significantly. During the TQ a strong $n = 2$ perturbation develops together with a broad band of weaker modes at higher n. Figure 5 shows the toroidal current density plotted in the injection plane at $\phi = 60°$ in the simulation with six gas injectors. In the pre-TQ and early TQ edge perturbations are seen that arise due to the presence and toroidal periodicity of the injected impurities. In these phases toroidal eddy currents are formed in the inner vacuum vessel in between the port regions, where such currents are suppressed due to anisotropic resistivity. In the late TQ the plasma becomes stochastic, which coincides with the onset of a broad spectrum of toroidal modes seen in figure 4(*b*).

The initial stored energy of this SPARC PRD equilibrium is $W_{\text{th}} = 20\,\text{MJ}$. In the simulations this energy is lost via radiation due to atomic processes as modeled with KPRAD, but also through thermal conduction through the first wall (red line in figure 2). The amount of energy that is lost via conduction strongly depends on the value of thermal conductivity κ that is imposed on the plasma. Within the extended-MHD model κ is not calculated self-consistently, but provided based on empirically determined values. Throughout most of the simulations and where not otherwise stated we use a value of $\kappa = 1.54 \times 10^{21}\,\text{m}^{-1}\,\text{s}^{-1}$ for isotropic thermal conductivity, while parallel thermal conductivity is set to a value of $\kappa_{\parallel} = 1.54 \times 10^{26}\,\text{m}^{-1}\,\text{s}^{-1}$. Figure 6 shows the temporal evolution
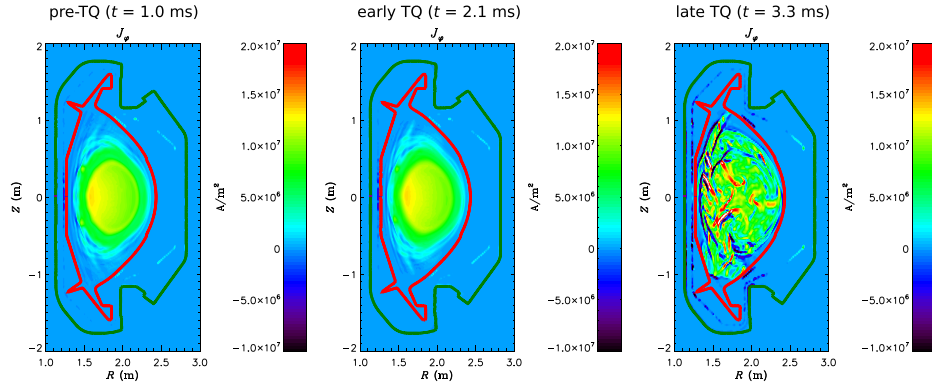
Figure 5. Toroidal current density in the pre-TQ, early TQ and late TQ is shown in the injection plane at $\phi = 60°$ for the simulation with six injectors.

of the total radiated power in all considered injector scenarios ranging from one to the maximum of six injectors[5]. Small sudden bursts of radiation are seen in the pre-TQ throughout all cases. While it is not entirely clear what causes these bursts, one explanation could be the cold injected gas reaching rational flux surfaces where it is rapidly transported along the field lines and thus able to radiate promptly. Nevertheless, as can be seen from figure 6(*b*) these radiation spikes do not lead to a noticeable loss of thermal energy, and thus do not matter for the overall energy balance. In the pre-TQ the loss of thermal energy is seen to scale with the number of injectors and thus also the total rate of injected impurities. The onset of the sawtooth starting at < 1 ms also does not correlate with an increase in radiated power. This can be explained by a lack of impurity mixing, as the impurities were not transported to the core and remain at the plasma edge at this early point in time. It can be seen in figure 6(*b*) that the one and five injector cases loose their thermal energy more rapidly than the other cases. This is a result of numerical difficulties in these simulations that required the isotropic thermal conductivity to be raised to a value of $\kappa = 1.39 \times 10^{22}\,\mathrm{m^{-1}\,s^{-1}}$ during the early TQ to get converged results. This increased the loss of energy by means of conduction through the first wall. These difficulties were not seen in the two and six injector simulations, where a radiative TQ is observed. In the two cases at the full nominal injection rate, i.e. two injectors and six injectors the initial stored thermal energy is lost within $\approx 4\,\mathrm{ms}$ after injection started. With six injectors, however, a small amount of energy is lost through conduction in the pre-TQ as a result of imposing a temporarily larger κ in this phase. Despite starting the actual TQ from a lower W_{th} with six injectors the TQ finishes about 0.2 ms later than in the two injector case. With 6 injectors it takes the plasma slightly longer to loose all of its thermal energy compared with 2 injectors and P_{rad} peaks at a later time,

as seen from figure 6. At the end of the TQ radiated power is still large, which is due to a conversion of Ohmic heating to radiation. In both cases more than 95% of the energy are radiated, while only about 2.1 MJ are conducted through the wall.

3.2. Current quench

Towards the end of the TQ an increase in plasma current is observed between 3 ms and 4 ms just before the start of the CQ. The toroidal current as a function of time is shown in figure 6(*c*). In both scenarios the CQ is very fast with a duration of only about 2.2 ms in the case of two injectors and 2 ms with six injectors, respectively. The observed CQ is faster than the prediction of the ITPA scaling [29], which yields a minimum CQ duration of 3 ms for the given SPARC equilibrium. However, we find that T_{e} drops rapidly with the onset of the CQ and during the second half of the CQ T_{e} reaches values below 6 eV, which is smaller than the values of T_{e} that were seen in experiments for example on EAST [30]. The rapid drop of T_{e} observed in the simulation together with the low value of T_{e} towards the end of the CQ would lead to increased plasma resistivity according to the Spitzer resistivity model and could explain the fast CQ. M3D-C1 modeling of KSTAR found shorter CQ durations than seen empirically [31]. Further validation of the predicted CQ durations in M3D-C1 is a topic of future works. At 6 ms, when the toroidal current is close to zero, the KPRAD module was switched off and at the same time the plasma viscosity was increased drastically in M3D-C1 to terminate the plasma dynamics with the aim to speed up the simulation and calculate the wall forces in the post-CQ.

3.3. Wall forces during and after rapid shutdown

There is no substantial vertical movement of the plasma during the rapid shutdown, i.e. we observe neither a hot or cold vertical displacement event (VDE). This is shown in figure 7 for the simulations with two and six injectors. The quantity shown here is the vertical position of the current centroid, which can

---

[5] Note that the cases with one, four and five injectors experienced difficulties converging around the start of the TQ and were not continued as the cases with two and six injectors represent injection from one and three toroidal locations, respectively. The case with four injectors at two toroidal positions was considered an alternative scenario, and with its toroidal spacing of 180° it would have required repositioning the DMS on the device.
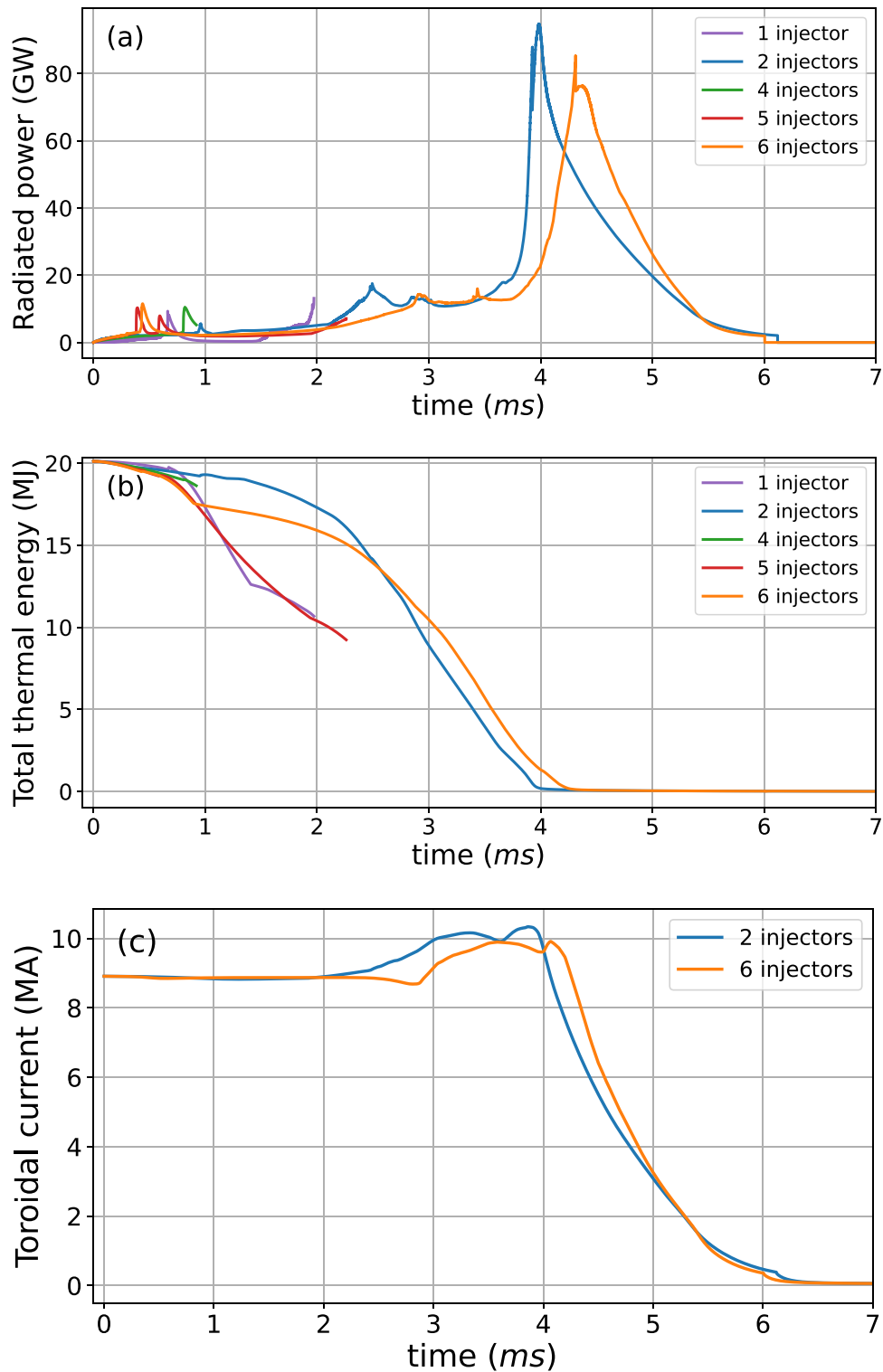
Figure 6. Radiated power (*a*) and thermal energy (*b*) vs. time for different injector configurations ranging from one to six injectors. Small transient radiation spikes occur in the pre-TQ in all cases. Radiated power during the TQ and CQ is shown for the cases with two and six injectors. (*c*) Total toroidal current inside the plasma domain shown for the two and six injector cases at the same injection rate.

be challenging to determine depending on the magnetic geometry. With six injectors this code diagnostic indicates a maximum vertical displacement of about 10 cm, which is smaller

than the vertical displacement of 24 cm with only two injectors. However, Poincare plots show an even smaller vertical displacement of only a few cm in both cases. The absence of a
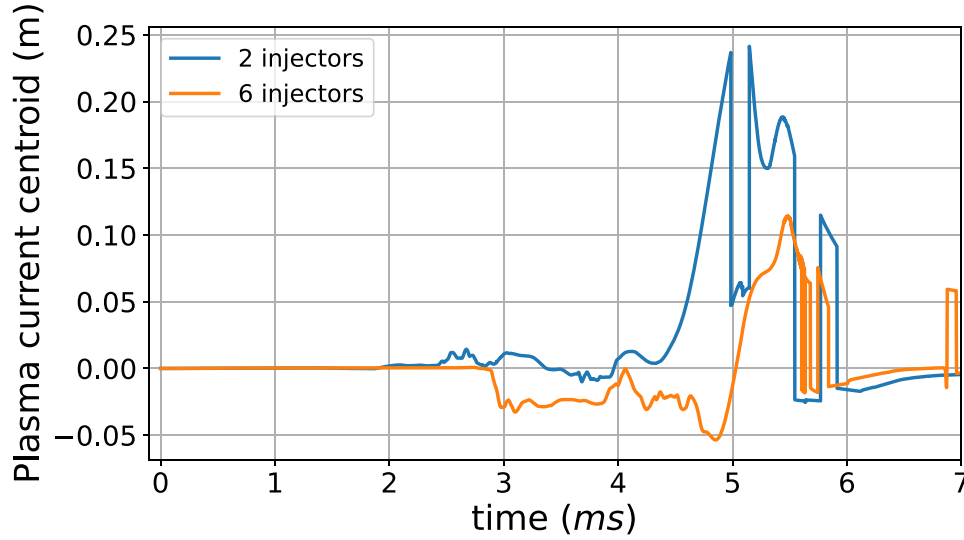
Figure 7. Comparison of the vertical position of the plasma current centroid in the simulations with two and six injectors.
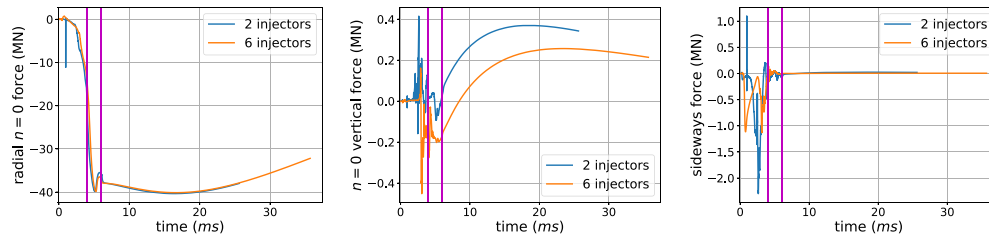

Figure 8. Total axisymmetric and non-axisymmetric forces inside the wall region. The vertical lines indicate the beginning and end of the current quench.

VDE is beneficial for the forces on the plasma vessel as eddy currents as well as halo currents associated with the vertical plasma motion are absent.

Overall, the forces on the vessel structure are moderate as seen in figure 8, which shows the horizontal and vertical axisymmetric force, as well as the non-axisymmetric sideways force integrated over the wall region. The strongest force is the axisymmetric radial force, which peaks at 40 MN during and after the CQ and points inwards in both injector cases. After the peak, the force is seen to slowly decay, which is consistent with the projected wall time of ∼50 ms on SPARC. The axisymmetric vertical force is two orders of magnitude smaller than the radial force, and thus differences between the two injector and six injector cases can be ignored. The non-axisymmetric sideways force (in horizontal direction) differs in the two considered injector scenarios. With only two injectors the force reaches peak values of above 2 MN, whereas with the full six injector layout the force is only about half of this value. However, the sideways force is one order of magnitude smaller than the axisymmetric radial force and thus in terms of the wall forces the six injector case performs only marginally better.

4. Spatial distribution of impurities and radiation

4.1. Localization of impurities and radiation

In the simulations it is seen that the injected impurities stay localized around the sites where the gas was injected. Figure 9 shows electron density n_e and radiated power P_{rad} at the plane of injection at different times during the simulation. While the size of the impurity cloud increases somewhat in size over time, there is no considerable radial, toroidal nor poloidal transport of the impurities throughout the TQ. As mentioned before, impurities are injected at zero temperature and then heated by the bulk plasma. Since the simulations use a single-fluid model, there is no ambipolar electric field resulting from electron pressure gradients, which might drive propagation of impurities to the surrounding plasma [32]. The instantaneous temperature equilibration causes a local decrease in temperature and pressure at the injection sites thus keeping the injected impurity atoms from spreading. Furthermore, toroidal equilibrium rotation is not considered in these simulations as simulation time was limited and the incomplete physics basis on rotation braking following MGI challenged the development of a
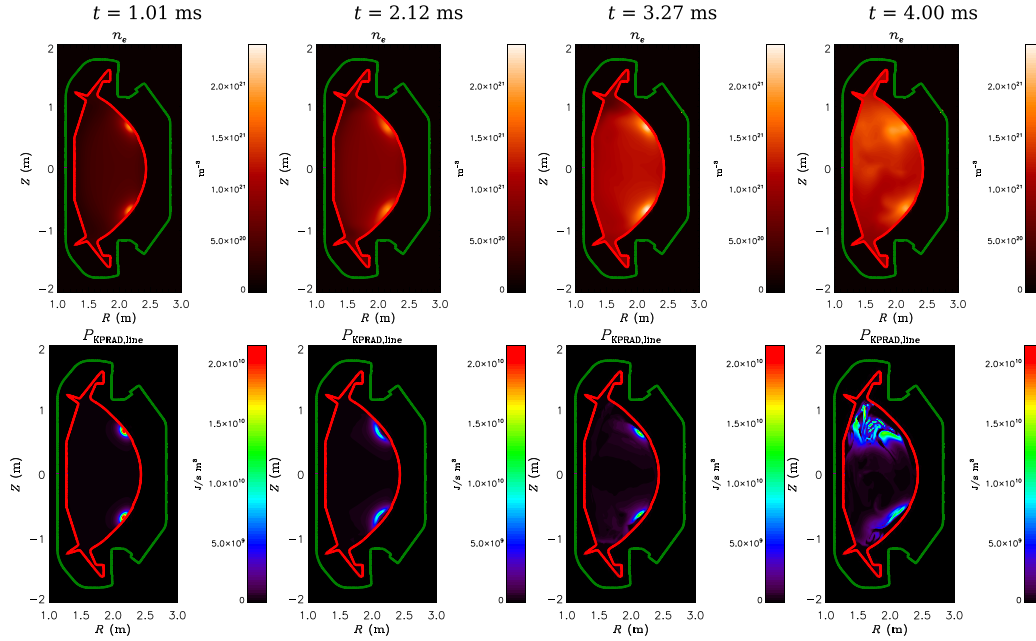
Figure 9. Electron density (top) and radiated power (bottom) shown for the six-injector case at the $\phi = 60°$ injector plane at different times.

reduced model. If finite equilibrium rotation was included, the impurities would be expected to better distribute along the flux surfaces in toroidal direction leading to less accumulation and also lower toroidal peaking as is discussed in the next section.

4.2. Toroidal peaking of radiation

To estimate the toroidal spread of radiation and to get an estimate on peak radiative heat loads on the first wall we calculate the TPF for radiated power. At a given time t the TPF can be defined as the peak value of the radiation field integrated in the poloidal plane at any toroidal location divided by the toroidal average

$$TPF = \frac{\left[\iint P_{\text{rad}}(R, \phi, Z)\, dRdZ\right]_{\text{peak}}}{\frac{1}{K}\sum_k \iint P_{\text{rad}}(R, \phi, Z)\, dRdZ}, \qquad (2)$$

where P_{rad} is the radiated power, K is the number of equidistant toroidal planes used to evaluate the TPF and k is an index that labels these planes. Note that the toroidal planes in the above equation are different from the (non-equidistant) toroidal planes in the M3D-C1 simulations. The finite elements used in M3D-C1 allow the radiation field to be evaluated at any toroidal angle and the calculation of the TPF is performed using equidistant toroidal angles with $K = 16$ and $K = 24$ for the two and six injector cases, respectively. These values are chosen to ensure that the toroidal angles where the radiation field is evaluated coincide with the locations of impurity injection. To evaluate radiation distribution in the different injector cases, we will calculate the TPF as a function of time to determine its overall maximum value, but also its value at the time of peak radiated power. Note that this method does not determine the magnitude of heat loads across the surface area

of the first wall, which can be calculated via ray tracing and is beyond the scope of this work. However, the calculated radiation fields can be used as input to ray tracing codes to map out the radiation loads at each point of the wall. Calculating the TPF is nevertheless an appropriate measure to evaluate the effect of different injector configurations on the toroidal peaking of radiation.

Figure 10(*a*) shows the TPF as a function of time in simulations with two and six injectors at the same nominal injection rate. At the beginning of the injection at $t = 0$ the TPF is very large, as the impurities are most localized (and so is radiation) at this moment. Since the total amount of impurities in the plasma is very small at this early stage, P_{rad} is low enough for the TPF to not be of concern. As can be seen by comparing figures 4 and 10 the TPF is not correlated with MHD activity. This can be explained by poor impurity mixing into the plasma core. The TPF drops rapidly and remains mostly at values of $2 - 4$ during the pre-TQ and early TQ. After a short increase to a value of 4 during the TQ in the six injector case, the TPF reduces to values of about 1.5–2.5 at the time when radiated power peaks and radiated power would be the most damaging. When only two injectors are used the TPF is considerably larger at a value of 7, which is reached when the total radiated power peaks. Hence, using the six injector configuration leads to more equally distributed heat loads than using only two injectors. Heat loads are most dangerous to plasma-facing components when they are peaked at a moment when the radiated power is large. Thus, the product of these two quantities provides a good estimate of how dangerous the heat loads are in the different injector configurations. This is illustrated in figure 10(*b*), and it can be seen that with only two injectors the heat loads are more concentrated and six injectors perform more favorably. We recall that in these simulations
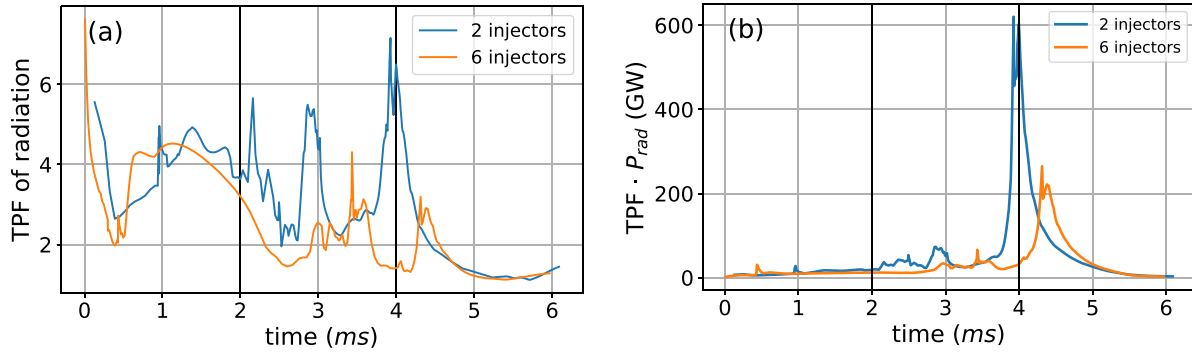
Figure 10. (*a*) Toroidal peaking factor (TPF) of radiation vs. time and (*b*) TPF multiplied by the radiated power P_{rad} in simulations with two and six injectors at the same total injection rate. The vertical black lines indicate the approximate beginning and end of the thermal quench.
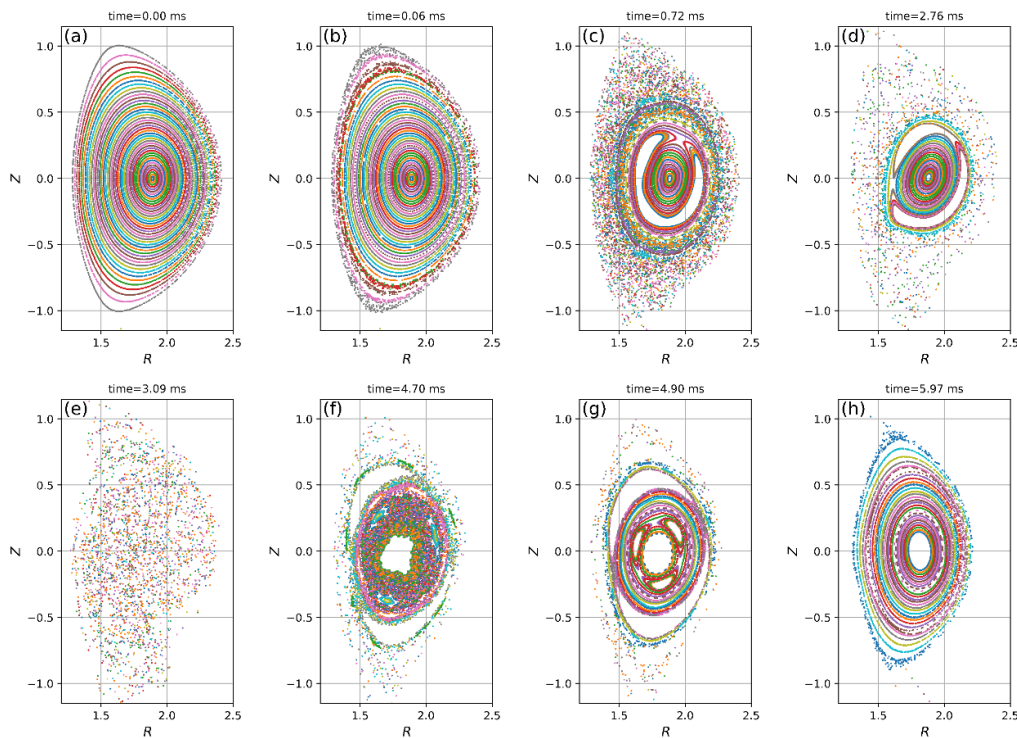

Figure 11. Evolution of the magnetic topology in the simulation with six gas injectors. (*a*) Equilibrium flux surfaces. (*b*) Shortly after gas injection has started. (*c*) Formation of the 1/1 island due to $q = 1$. (*d*) Stochastization reaching 1/1 island in early TQ. (*e*) Full stochastization during TQ. (*f*) Magnetic island chains form in the core during CQ. (*g*) Closed flux surfaces re-appear. (*h*) Mostly reformed flux surfaces near the end of the CQ.

the impurities are advected by bulk plasma flow only. Since the impurities are injected at zero temperature there is no local increase in pressure and with the absence of an ambipolar electric field the TPF is overestimated and will likely be lower. This effect could be included in two-fluid simulations, which are reserved for future work. In addition, equilibrium toroidal rotation is zero. Another contributing factor to a high TPF is the zero initial velocity of the injected impurities, which keeps the impurities from further spreading radially into the plasma core. All of these effects would lead to a stronger motion of impurity particles away from the injector sites and a further reduction of the TPF could be expected when these effects were included. This should be subject of future simulations.

5. Evolution of the magnetic topology

The magnetic topology during a rapid shutdown can affect the formation of runaway electrons [33, 34]. While a detailed study of the formation of runaway electrons is beyond the scope of this work, in this section we will provide insight on the evolution of the magnetic flux topology throughout the rapid shutdown, which is useful for future investigations on the matter.

The analysis in this section focuses on the case with six gas injectors, since this is the preferred configuration as discussed in the previous section. The evolution of the magnetic topology is visualized in figure 11. It is seen that upon injection

of the gas a stochastic region forms in the outer region of the plasma. After initial growth the size of this stochastic region remains constant until 0.7 ms, when a magnetic island forms in the core (figure 11(*c*)). The formation of this island coincides with sawtooth onset as seen from figure 4. During the pre-TQ and in the early TQ the magnetic field stochasticizes further inwards until reaching the location of the 1/1 magnetic island (figure 11(*d*)). At 3 ms the magnetic field is fully stochastic (figure 11(*e*)) before the magnetic surfaces start to reform during the CQ. A large $m = 2$ magnetic island can be seen at 4.7 ms in the outer part of the plasma together with other island chains in the core (figure 11(*f*)). Closed flux surfaces appear shortly after (4.9 ms) as shown in figure 11(*g*). During the late CQ more flux surfaces reform throughout the plasma volume with the 2/1 island moving towards the magnetic axis before the flux surfaces are restored (figure 11(*h*)).

It is known that runaway electrons are generated around the plasma edge during impurity injection [35]. It was previously observed that stochastic field lines in the outer part of the plasma can lead to the loss of REs to the wall [36]. Typically, in a stochastic region runaway electrons diffuse out of the plasma faster than thermal particles, as a stochastic field region cannot contain such energetic electrons. However, the formation of the magnetic 1/1 island during the pre-TQ might act to retain some runaway electrons and potentially lead to an avalanche with associated runaway current before it disappears when the whole plasma domain becomes stochastic. During the CQ, when the flux surfaces are restored, a runaway population could potentially build up in the magnetic islands and avalanche. A detailed study of natural runaway formation in SPARC might be performed in a future M3D-C1 study.

6. Conclusions

Extended-MHD simulations of rapid plasma shutdowns via MGI in SPARC were performed with the M3D-C1 code. Recent developments to the meshing capabilities allow for a more realistic representation of conducting elements surrounding the plasma as well as narrower gas plumes, and thus enable higher fidelity simulations with narrower gas jets and more realistic wall forces. We have demonstrated that M3D-C1 can model a rapid shutdown via MGI with narrow and more realistic gas plumes in SPARC. This was done using toroidal mesh packing around the injector locations to resolve the associated strong gradients as well as temporary adjustments in heat conductivity and density diffusion during the pre-TQ. While the temporary increases in heat conductivity and density diffusion lead to increased losses through thermal conductivity to the wall, these losses were kept small enough to still obtain a radiative shutdown of the plasma and more than 95% of the thermal energy was radiated. Neither a hot or cold VDE is observed in the MGI simulations. This is beneficial for the wall forces, which peak at 40 MN for the radial force. The only considerable difference between the two and six injector cases in terms of wall forces

is seen for the sideways force, which is twice as large with only two injectors. However, since the sideways force is one order of magnitude below the radial force this difference is marginal.

Due to a lack of impurity mixing into the core the sawtooth instability has no effect on radiation. We find that using the maximum of six gas injectors leads to a more even distribution of radiation toroidally than using two injectors located at the same toroidal angle. While the TPF in this scenario is still slightly higher than desired, it can be expected that in a real plasma toroidal peaking would be lower. This is due to the lack of toroidal rotation, non-zero initial velocity of the gas plume and a local pressure dip due to the impurities being injected at zero temperature. The inclusion of these additional physics, which would be present in a real plasma, can contribute to a lower TPF. Nevertheless, the TPF predicted by these simulations is still low enough to suggest that MGI with six gas valves positioned at three toroidal locations is an effective way to rapidly shut down the plasma in SPARC.

Data availability statement

The data that support the findings of this study are openly available at the following URL/DOI: https://doi.org/10.34770/2b26-tb11.

ORCID iDs

A. Kleiner ⓘ https://orcid.org/0000-0002-5800-8027
N.M. Ferraro ⓘ https://orcid.org/0000-0002-6348-7827
R. Sweeney ⓘ https://orcid.org/0000-0003-3408-1497
B.C. Lyons ⓘ https://orcid.org/0000-0003-3232-1581
M. Reinke ⓘ https://orcid.org/0000-0003-4413-9613

References

[1] Boozer A.H. 2012 *Phys. Plasmas* **19** 058101

[2] de Vries P., Johnson M., Alper B., Buratti P., Hender T., Koslowski H. and Riccardo V. Contributors J E 2011 *Nucl. Fusion* **51** 053018

[3] Whyte D., Minervini J., LaBombard B., Marmar E., Bromberg L. and Greenwald M. 2016 *J. Fusion Energy* **35** 41–53

[4] Creely A.J. *et al* 2020 *J. Plasma Phys.* **86** 865860502

[5] Creely A.J., Brunner D., Mumgaard R.T., Reinke M.L., Segal M., Sorbom B.N. and Greenwald M.J. 2023 *Phys. Plasmas* **30** 090601

[6] Sweeney R., Creely A.J., Doody J., Fülöp T., Garnier D.T., Granetz R., Greenwald M., Hesslow L., Irby J. and and I.V.A. *et al* 2020 *J. Plasma Phys.* **86** 865860507

[7] Rodriguez-Fernandez P. *et al* 2022 *Nucl. Fusion* **62** 042003

[8] Whyte D. *et al* 2003 *J. Nucl. Mater.* **313–316** 1239–46

[9] Lehnen M. *et al* contributors J E 2011 *Nucl. Fusion* **51** 123010

[10] Reinke M., Whyte D., Granetz R. and Hutchinson I. 2008 *Nucl. Fusion* **48** 125004

[11] Olynyk G. *et al* 2013 *Nucl. Fusion* **53** 092001

[12] Baylor L. *et al* 2009 *Nucl. Fusion* **49** 085013

[13] Commaux N., Baylor L., Jernigan T., Hollmann E., Parks P., Humphreys D., Wesley J. and Yu J. 2010 *Nucl. Fusion* **50** 112001

[14] Whyte D., Granetz R., Bakhtiari M., Izzo V., Jernigan T., Terry J., Reinke M. and Lipschultz B. 2007 *J. Nucl. Mater.* **363–365** 1160–7

[15] Ferraro N., Lyons B., Kim C., Liu Y. and Jardin S. 2018 *Nucl. Fusion* **59** 016001

[16] Lyons B.C., Kim C.C., Liu Y.Q., Ferraro N.M., Jardin S.C., McClenaghan J., Parks P.B. and Lao L.L. 2019 *Plasma Phys. Control. Fusion* **61** 064001

[17] Schwarz N. *et al* (the ASDEX Upgrade Team, JET Contributors and the JOREK Team) 2023 *Nucl. Fusion* **63** 126016

[18] Artola F.J., Sovinec C.R., Jardin S.C., Hoelzl M., Krebs I. and Clauser C. 2021 *Phys. Plasmas* **28** 052511

[19] Clauser C., Jardin S. and Ferraro N. 2019 *Nucl. Fusion* **59** 126037

[20] Izzo V. *et al* 2015 *Nucl. Fusion* **55** 073032

[21] Clauser C., Jardin S., Raman R., Lyons B. and Ferraro N. 2021 *Nucl. Fusion* **61** 116003

[22] Whyte D.G. *et al* 1997 *Proc. of 24th European Conf. on Controlled Fusion and Plasma Physics* vol 21A pp 1137–40

[23] Izzo V., Sweeney R.M., Tinguely R.A., Battey A.F. and Hansen C.J. 2024 Predictive modeling for successful disruption mitigation on SPARC *Invited Talk at the 66th Annual Meeting of the APS Division of Plasma Physics (Atlanta, GA, 7 October 2024)*

[24] Body T., Hasse C. and Creely A. 2023 The SPARC primary reference discharge defined by cfsPOPCON (https://doi.org/10.48550/arXiv.2311.05016)

[25] Breslau J., Ferraro N. and Jardin S. 2009 *Phys. Plasmas* **16** 092503

[26] Jardin S. 2004 *J. Comput. Phys.* **200** 133–52

[27] Jardin S., Breslau J. and Ferraro N. 2007 *J. Comput. Phys.* **226** 2146–74

[28] Hulse R.A. 1983 *Nucl. Technol.* **3** 259–72

[29] Eidietis N. *et al* 2015 *Nucl. Fusion* **55** 063030

[30] Chen D.L., Shen B., Yang F., Qian J.P. and Xiao B.J. 2015 *Chin. Phys.* B **24** 025205

[31] Lyons and B. *et al* 2024 Validation of extended-magnetohydrodynamic modeling of disruption mitigation with collisional-radiative impurities *Presented at the Sherwood Fusion Theory Conf. 2024 (Missoula, MT)*

[32] Mao H., Zhang Y. and Tang X. 2023 Rapid assimilation of high-z impurity ions along the magnetic field line from an ablated pellet (arXiv:2311.09396)

[33] Carbajal L., del Castillo-Negrete D. and Martinell J.J. 2020 *Phys. Plasmas* **27** 032502

[34] Sommariva C., Nardon E., Beyer P., Hoelzl M., Huijsmans G., van Vugt D. and Contributors J. 2017 *Nucl. Fusion* **58** 016043

[35] Vallhagen O., Embreus O., Pusztai I., Hesslow L. and Fülöp T. 2020 *J. Plasma Phys.* **86** 475860401

[36] Liu C., Zhao C., Jardin S.C., Ferraro N.M., Paz-Soldan C., Liu Y. and Lyons B.C. 2021 *Plasma Phys. Control. Fusion* **63** 125031